

1 **Supplementary Information for “A Radiometrically Dated Record of Antarctic Ice Sheet**  
2 **Response to Millennial-Scale Climate Cycles during Glacials and Interglacials”** by G.  
3 Piccione, T. Blackburn, S. Tulaczyk, E.T. Rasbury, M. Hain, D.E. Ibarra, K. Methner, C. Tinglof,  
4 B. Cheney, P. Northrup<sup>2</sup>, K. Licht  
5

6 **<sup>234</sup>U-<sup>230</sup>Th dating**

7 <sup>234</sup>U-<sup>230</sup>Th dates were produced at the University of California Santa Cruz (UCSC) Keck Isotope  
8 Laboratory. Samples were spiked with a gravimetrically calibrated mixed <sup>229</sup>Th-<sup>236</sup>U tracer for isotope  
9 dilution analyses. They were then digested in 3mL 7N HNO<sub>3</sub> (calcite) or concentrated 4mL HF + HNO<sub>3</sub>  
10 (opal) via benchtop dissolution and dried down. U and Th separates were purified using ion chromatography  
11 with 1mL columns of 200-400 mesh, AG1-X8 anion resin. Samples were loaded onto the column in 1mL  
12 of 7N HNO<sub>3</sub> and major elements were washed off with an additional 2ml HNO<sub>3</sub>. Loading and washing  
13 eluant was collected and saved for Sr analyses. Thorium was eluted in 2mL of 6N HCl. Uranium was then  
14 eluted in 2mL of ultra-pure water. This column procedure was then repeated to achieve U and Th purity  
15 levels necessary for analyses. Total procedural blanks were <10pg for U and <25pg for Th, which are minor  
16 relative to sample concentrations. Both U and Th isotopic measurements were conducted using the IsotopX  
17 X62 Thermal Ionization Mass Spectrometer (TIMS) housed at UCSC. U and Th samples are loaded onto  
18 99.99% purity Re ribbon. Uranium is loaded in a Si-gel activator and measured as UO<sub>2</sub>. Uranium  
19 compositions were corrected for oxide isobaric interferences following ref.<sup>1</sup>. Uranium measurements were  
20 performed as a two sequence “Fara-Daly” routine: in the first sequence, <sup>234</sup>U (mass 266) is collected on the  
21 Daly, while <sup>235</sup>U (mass 267) and <sup>238</sup>U (mass 270) is collected on the high Faraday cups equipped with 1e<sup>12</sup>  
22 Ω resistors. The second sequence placed <sup>235</sup>U (mass 267) on the Daly and <sup>236</sup>U (mass 268) and <sup>238</sup>U (mass  
23 270) on the high Faraday cups. The 266(Daly)/270(Faraday) composition was corrected using the Fara-  
24 Daly gain: (267Faraday/270Faraday) / (267Daly/270Faraday). Uranium compositions were corrected for  
25 oxide isobaric interferences following ref.<sup>1</sup>. Mass dependent fractionation correction was applied using a  
26 linear correction with correction factor determined from long-term measurement of standards. Uranium  
27 dead times for the Daly were calibrated using NBS U-500. Accuracy of the uranium method is evaluated  
28 using Uranium standard NBS4321 (Extended Data Fig. 10). Thorium isotope measurements were also done  
29 on the TIMS at UCSC. Thorium is loaded in a graphite emitter and measured as a metal. Each mass of Th  
30 is measured using a peak hopping routine on the Daly. Thorium fractionation and deadtime were estimated  
31 by running NBS U-500 as a metal. Accuracy of <sup>234</sup>U-<sup>230</sup>Th dates were tested using MIS 5e coral and  
32 compared to dates in ref<sup>2</sup>, as well as a previously dated carbonate precipitate<sup>3</sup>. U-Th ages are calculated  
33 using codes designed at UCSC. All ages are corrected for initial [<sup>230</sup>Th/ <sup>232</sup>Th] assuming a composition of  
34 4.4±2.2e-6. As the exact [<sup>230</sup>Th/ <sup>232</sup>Th]<sub>i</sub> is unknown, we assume this ratio from the expected composition  
35 of the silicate upper crust in secular equilibrium, allowing for a departure from this composition of 50%,  
36 and propagating this uncertainty through to the final age. Decay constants for all data and models were  
37 from ref. <sup>4</sup>. All uncertainties are reported at 2σ, unless otherwise specified.

38 **Subglacial precipitate source areas**

39 In the main text, we have briefly discussed the potential source areas of the two precipitate samples: MA113  
40 and PRR50489. Here, we provide further relevant details.

41 Sample MA113 is found at Mount Achernar Moraine (henceforth MAM; 84.2°S, 161°E), a nearly  
42 motionless body of blue ice on the side of Law Glacier, with average surface velocity of about 25 m a<sup>-1</sup> <sup>5</sup>.  
43 The moraine is located ca. 20 km downstream of the polar plateau, and its debris is derived locally, with  
44 Beacon and Ferrar Supergroup rocks dominating the sample collection area. The subglacial origin of the  
45 geologic material is supported by an abundance of striated and faceted clasts<sup>6</sup>. Subglacial debris is  
46 transported to the surface of MAM with upward-flowing ice from the depths of Law Glacier, and is then  
47 deposited on the surface as the surrounding ice sublimates (e.g., figure 9 in ref. <sup>6</sup>). Graly et al. (2018)  
48 inferred that the most plausible mechanism of subglacial entrainment of the debris is regelation in an open

49 hydrological system and assessed that suitable conditions for this process exist 30-50 km upstream from  
50 the moraine<sup>7</sup>. The length of time for the emergence of basal debris to MAM is estimated to be at least 35  
51 ka<sup>6</sup>, which is close to the youngest radiometric U-series age obtained for sample MA113 ( $25.44 \pm 0.59$  ka).  
52 The similarity between the two timescales supports the possibility that the sample formed in a location  
53 much more proximal to MAM than 30-50 km, perhaps in one of the overdeepenings in Law Glacier valley  
54 that can be found within several kilometers of the moraine (e.g., Figure 7 in ref. <sup>5</sup>). Such an overdeepening  
55 represents a suitable setting for precipitate formation because the catchment geometry would allow  
56 subglacial waters to become isolated and overconcentrated to the point of opal precipitation during regional  
57 basal freezing periods and millennial cold phases. Calcite precipitation may occur as the regional basal  
58 water system reconnects to the overdeepening during the regional expansion of basal melting, which is  
59 associated with warm AIM phases in our model (Extended Data Fig. 8). Whereas we cannot pinpoint the  
60 exact location from which the sample MA113 originated, we conjecture that it was formed in a subglacial  
61 overdeepening located several kilometers to a few dozens of kilometers upstream of MAM.

62 Sample PRR50489 comes from Elephant Moraine (henceforth EM;  $76.3^{\circ}\text{S}$ ,  $157.3^{\circ}\text{E}$ ), a  
63 supraglacial moraine in a blue ice area of Transantarctic Mountains, where ice sublimation persisting for  
64 estimated  $\sim 100$  ka released debris from basal ice of the East Antarctic ice sheet<sup>8,9</sup>. The current sublimation  
65 rate in the area is ca.  $0.04$  m/year<sup>10</sup>. It is not yet proven what triggered the formation of EM, but it could  
66 have been related to a capture of the upper part of Mawson Glacier drainage by the southern tributaries of  
67 the David Glacier, which experienced vertical incision of hundreds of meters in the last 234 kyr<sup>11</sup>. This  
68 switch from eastward ice flow towards the modern Mawson Glacier to northward flow towards David  
69 Glacier could have aided the emergence of basal ice layers at the EM. In the discussions below, we will  
70 assume that at the time of PRR50489 formation, which predates the formation of the EM itself, ice upstream  
71 of the moraine was flowing towards Mawson Glacier. However, none of our fundamental inferences would  
72 change significantly if, instead, we assumed that the modern ice flow pattern (i.e., ice flow from EM north  
73 towards David Glacier) prevailed then.

74 Rock lithologies found on the surface of EM include material from the Beacon and Ferrar  
75 Supergroups and some Tertiary fragments with Neogene marine microfossils, interpreted to have come  
76 from the subglacial Wilkes Basin located to the west of the mountain range<sup>12</sup>. We use the simple method  
77 employed in ref. <sup>5</sup> to estimate the time needed for our subglacially formed sample to emerge from the bed  
78 through 1.5-2.0 km of ice, which are the typical ice thicknesses upstream of EM in the Bedmap2 dataset<sup>13,14</sup>.  
79 To approximate the emergence timescale, we divide ice thickness by the sublimation rate and get a range  
80 of ca. 40-50 ka. To glean information about the precipitate source area from this emergence timescale, we  
81 must also account for the time that the sample may have spent laying on the surface of EM. Cosmogenic  
82 surface exposure ages of EM boulders were measured to be up to 60 ka<sup>15</sup>, and meteorites found nearby  
83 have exposure ages up to 100s of thousands of years<sup>16</sup>. Given the significant uncertainties associated with  
84 the emergence timescale and the surface-residence timescale for this sample that was still precipitating in  
85 subglacial water <145 kyr ago, we conservatively assume a wide temporal range, 10-100 kyr, for the period  
86 it spent both traveling horizontally in basal ice and sitting on top of the moraine. Whereas the ice surface  
87 velocity over EM itself is very slow ( $<0.1$  m/yr)<sup>8</sup>, the proximal upstream part of the southern drainage area  
88 of David Glacier moves at ca.  $5$  m/yr<sup>17</sup>. Using the modern flow configuration<sup>18,19</sup>, the longest ice flowline  
89 reaching EM from the regional ice divide separating drainage basins of David and Mulock Glaciers is ca.  
90 150 km. In theory, our sample could have traveled from this area if its average velocity over our assumed  
91 upper bound for horizontal travel (100 kyr), was  $1.5$  m/yr. However, this is likely to be too large an average  
92 basal transport velocity to assume over such an extended period, which includes cold glacial conditions  
93 with accumulation rates, and hence also balance ice velocities, that were 2-3 times lower than Holocene  
94 rates<sup>20</sup>. In addition, a debris fragment embedded in basal ice travels at velocities lower than the surface ice  
95 velocity. For instance, in their analysis of basal debris transport to MAM, Kassab et al. (2019) assumed an  
96 average basal transport velocity of  $0.5$  m/yr even though ice surface velocities within Law Glacier are about  
97  $25$  m/yr<sup>5</sup>. In the slower flowing region (surface velocity of  $5$  m/yr) upstream of EM this would be equivalent  
98 to basal transport velocity of  $0.1$  m/yr. At such speed, our sample would have traveled only 1-10 km in the  
99 assumed period of horizontal transport ranging from 10 to 100 kyr. We conjecture that PRR50489 formed

100 in a basal overdeepening within a relatively small range away from EM. Although the horizontal resolution  
101 of Bedmap2 bed topography is worse here than in the vicinity of MAM, it contains an indication of a broad  
102 overdeepening that starts a few kilometers upstream of EM.

103

#### 104 **Reduced complexity ice sheet model**

105 We use a reduced complexity model of ice thermodynamics to demonstrate that there is a glaciologically  
106 plausible mechanism for explaining the two key observations derived from the precipitate samples MA113  
107 and PRR50489: (i) cyclic opal-calcite precipitation from subglacial waters switching between oxygen- and  
108 carbon-poor brines and carbon- and oxygen-rich meltwaters, and (ii) the correlation between opal  
109 precipitation and millennial cold phases, and between calcite layers and millennial warm phases. Combined,  
110 these observations indicate that the subglacial water bodies in which these two samples formed, although  
111 separated by nearly 1000 km distance, experienced hydrologic isolation and cryoconcentration during  
112 millennial cold phases and became open to basal meltwater inputs during warm phases. Glaciologically,  
113 the most parsimonious explanation is that the cold millennial phases corresponded to basal freezing  
114 conditions, while warm phases to basal melting conditions in the two areas of sample formation.

115 Our modeling approach is inspired by the simplicity of the binge-purge model of Heinrich events<sup>21</sup>.  
116 In fact, initially we considered the binge-purge model to be a potential explanation for the millennial-scale  
117 opal-calcite couplets found in our samples due to the shared millennial-scale periodicity of both. However,  
118 the fundamental problem with this interpretation is that the binge-purge model predicts millennial-scale  
119 switches between basal freezing and melting for the Hudson Bay ice stream assuming surface accumulation  
120 rates that are about one order of magnitude higher than the accumulation rates prevailing in our Antarctic  
121 study areas<sup>21-23</sup>. Hence, application of the binge-purge scaling (right-hand side of equation 12 in ref. <sup>21</sup>)  
122 with such small accumulation rates would yield unsatisfactorily high periodicity. Moreover, it would be a  
123 remarkable coincidence if a climatically unforced binge-purge oscillator, as proposed in ref. <sup>21</sup>, would result  
124 in the observed correspondence between the periods of opal and calcite precipitation, and cold and warm  
125 phases of AIM cycles at two locations very distant from each other (Fig. 1). Reconstructions of recent  
126 internally driven ice stream cyclicity in West Antarctica yield periodicities of hundreds of years, which are  
127 in turn much shorter than the AIM-scale ice dynamic variability needed to explain our observations<sup>24</sup>. Given  
128 these considerations, we formulate a reduced-complexity model of ice sheet thermodynamics to illustrate a  
129 glaciologically plausible link between millennial-scale climate forcing and subglacial precipitation of opal  
130 and calcite driven by changes in basal thermal regime. It is crucial to keep in mind that this model is used  
131 here solely for illustrative purposes. There are simply too many relevant observational uncertainties (e.g.,  
132 locations of sample precipitation, geothermal flux at these locations, ice thickness and ice flow history  
133 during sample precipitation, etc.) to constrain a more complex model aimed at reconstructing in detail ‘what  
134 really happened’ during sample precipitation. Instead, our goal is to illustrate a plausible mechanism with  
135 a simple model.

136 Switches between basal melting and freezing conditions are controlled by the basal thermal energy  
137 balance,  $E$ . The three most fundamental controls on  $E$  are two sources of heat ( $G$  = geothermal heat flow  
138 and  $S$  = shear heating accompanying ice motion), and one sink of heat ( $Q$  = conductive heat loss) (e.g., ref.  
139 <sup>25</sup>):

$$140 \quad 141 \quad E = G + S - Q \quad \text{Eq. S1}$$

142 There is no physical reason for geothermal heat flow to vary on the timescale of AIMs. Hence, we treat it  
143 as a time invariable parameter with a value of  $0.05 \text{ W/m}^2$  <sup>26</sup>. Changes in surface temperature and  
144 accumulation rate accompanying AIMs can impact the basal thermal energy balance through the conductive  
145 heat loss term,  $Q$ , but the ice sheet does mute this effect through<sup>21</sup>: (i) dampening the amplitude of  
146 temperature variations with depth, and (ii) introducing a time lag between surface climate forcing and basal  
147 thermal response. In ref. <sup>21</sup> authors pointed out that a under the purely conductive vertical heat transport, a  
148 periodic surface temperature forcing will decay exponentially with e-folding depth scale of 314 m. Given

149 that the potential sample source areas have ice thicknesses of about 1500m<sup>13,14,27</sup>, an AIM-scale surface  
 150 temperature fluctuations of 1-3°C<sup>28,29</sup> would amount to 0.008-0.025°C change in ice temperature near the  
 151 bed. Thicker ice would cause even more attenuation of the temperature signal and much thinner ice  
 152 thickness (e.g., 1000m) would result in our model always predicting basal freezing, rather than switches  
 153 between melting and freezing conditions at the ice base. Using equation 1 from ref. <sup>30</sup> we calculated that,  
 154 even assuming an instantaneous thermal equilibration throughout ice thickness, the maximum difference  
 155 between the conductive heat loss during cold and warm AIM phases would be about 0.001 W/m<sup>2</sup> (assuming  
 156 ice thickness of 1500m, temperature change of 3°C, and accumulation rate of 0.03 m/yr during the warm  
 157 phase and 0.02 m/yr during the cold phase<sup>31</sup>.) This is more than an order of magnitude less than the assumed  
 158 geothermal flux. We will show later that it is also one to two orders of magnitude less than the contribution  
 159 from the shear heating term, S.

160 The second fundamental problem with relying on vertical advection and diffusion of surface  
 161 climate signals to the bed is the significant time lag with which such a transfer happens (e.g., ref. <sup>21</sup>). The  
 162 timescale for purely conductive heat transfer can be estimated from the ratio of the square of ice thickness  
 163 (H) to the thermal diffusivity of ice, which for H of 1500 m and diffusivity of 44 m<sup>2</sup>/yr <sup>21</sup> yields ca. 50,000  
 164 years. The equivalent timescale for the purely advective vertical heat transfer can be approximated as the  
 165 ratio of the ice thickness to the surface accumulation, which for reasonable assumptions of 1500m and 0.03  
 166 m/yr <sup>31</sup>, respectively, also yields 50,000 years. The low accumulation rates assumed for the regions of  
 167 interest are justified by both ice sheet modeling of ice sheet sensitivity to AIM forcing<sup>27</sup>, and the fact that  
 168 the two samples were found in locations where under modern conditions the surface mass balance is  
 169 negative<sup>5,32</sup>. These low surface accumulation rates are also compatible with recent direct observations in  
 170 the study regions<sup>23</sup> and with reconstructions of accumulation rates from the Taylor Dome ice core<sup>22</sup>.  
 171 Although we have used one specific thickness, 1500 m, to calculate these hypothetical timescales, our  
 172 results would not substantially change if we would consider a wider range of thicknesses, e.g., 1000-2000  
 173 m, for which these timescales would also be in tens of thousands of years. Given that these diffusive and  
 174 advective time scales are about an order of magnitude longer than the millennial-scale AIM climate  
 175 fluctuations, we do not favor variations in the conductive heat loss term (Q in equation S1) as an explanation  
 176 for the cyclicity in subglacial hydrological conditions inferred from our samples.

177 By the process of elimination, we arrive at the shear heating term, S, in equation S1 as the most  
 178 promising mechanism for triggering switches between basal melting and freezing conditions on millennial  
 179 timescales. Given the slow ice motion at, and upstream of, sample collection locations<sup>14</sup>, we approximate  
 180 the shear heating term, S, as a product of the driving shear stress and deformational ice velocity, U, averaged  
 181 over ice thickness:

$$182$$

$$183 \quad S = \tau U = \frac{2A}{n+2} \tau^{n+1} H = \frac{2A}{n+2} (\rho g \alpha)^{n+1} H^{n+2} \quad \text{Eq. S2}$$

$$184$$

185 where  $\tau$  =gravitational driving stress ( $\rho g H \alpha$ ),  $\rho$  = ice density,  $g$  = gravitational acceleration,  $H$  = ice  
 186 thickness,  $\alpha$  = ice surface slope,  $n$  = stress exponent in the ice flow law (assumed to be 3, ref. <sup>33</sup>, table 3.3),  
 187 A = ice viscosity parameter (the value for ice at 0°C in the table 3.4 in ref. <sup>33</sup>). We follow the simplifying  
 188 assumption that all shear heating can be attributed to ice motion at/near the basal interface<sup>34</sup>. Equation S2  
 189 is based on shallow ice approximation assumption for an ice sheet moving through internal ice deformation.  
 190 These assumptions are justified based on the relatively modest ice surface velocities dominating the two  
 191 sample collection areas, MAM and EM, and the regions that feed ice into them from upstream<sup>14,18</sup>.

192 Equation S2 contains two glaciological variables that vary with climate forcing, the ice surface  
 193 slope and ice thickness. Since the latter is raised to a higher power ( $H^5$ ) than the former ( $\alpha^4$ ), perhaps ice  
 194 thickness is the preferred pathway through which millennial scale climate changes have influenced shear  
 195 heating in the two sample formation areas? However, to match the observed precipitation patterns, ice  
 196 thickness would have to increase during warm AIM phases and decrease during millennial cold phases. The  
 197 only published model of Antarctic ice sheet sensitivity to AIM climate forcing<sup>27</sup> shows the ice sheet  
 198 thickness decreasing with increasing temperature in both regions from which our samples have been

199 collected. This suggests that the tendency for the ice sheet to thicken as accumulation rate increase under  
 200 warming climates is overcome by an increase in the dynamic ice thinning associated with the grounding  
 201 line retreat and ice flow acceleration during warm AIM phases<sup>27</sup>. This is certainly consistent with the fact  
 202 that ice thicknesses decreased by hundreds of meters in Transantarctic Mountains<sup>35,36</sup> in response to climate  
 203 warming after the last glacial maximum even though accumulation rates roughly doubled<sup>20</sup>. Similarly,  
 204 Neuhaus et al. (2021) proposed that the grounding line in the Ross Embayment retreated when accumulation  
 205 rates increased and advanced when they fell during Holocene millennial-scale climate variations<sup>37</sup>.

206 The dynamic effect driving ice sheet evolution in response to ocean thermal forcing on grounding  
 207 lines is incorporated into our simplified model of shear heating (Equation S2) through the ice surface slope,  
 208 which steepens when the ice in the Ross Embayment thins during grounding line retreats (AIM warm  
 209 phases) and becomes shallower when ice sheet thickness in the Ross Embayment increases during  
 210 grounding line advances (millennial cold phases). In our calculations of time-dependent shear heating we  
 211 parametrize the evolution of regional ice surface slope along an ice drainage pathway connecting a sample  
 212 origination region to the Ross Embayment:

$$213 \alpha(t) = [\Delta b + H(t) - H_{RE}(t)]/L_o \quad \text{Eq. S3}$$

214 where  $\Delta b$  = bedrock elevation difference between the region from which a sample originated and the part  
 215 of the Ross Embayment into which ice from this region is draining (at the foothills of Transantarctic  
 216 Mountains),  $H(t)$  = ice thickness in the region of sample origin,  $H_{RE}(t)$  = ice thickness at the foothills of  
 217 Transantarctic Mountains (e.g., locations of the mouths of Law Glacier for the MAM sample and Mawson  
 218 Glacier for the EM sample),  $L_o$  = a length scale representing the distance between the sample origination  
 219 region and the ice discharge area in the Ross Embayment. Consistent with the simplicity of our model we  
 220 assume  $L_o$  to be ~100 km, which is approximately equal to the distance between MAM and EM locations  
 221 and the mouths of Law and Mawson Glaciers. The bedrock elevation difference is estimated from existing  
 222 bed elevation datasets<sup>13,14</sup> and our preferred locations of sample origin (see the discussion above). We have  
 223 run multiple sensitivity tests assuming different values of  $\Delta b$  and  $L_o$  and the results presented below and in  
 224 the main manuscript are not fundamentally dependent on the preferred values stated here being exact. The  
 225 model produces the desired switches between basal melting and freezing for wide ranges of  $\Delta b$  and  $L_o$ .  
 226 The model produces the desired switches between basal melting and freezing for wide ranges of  $\Delta b$  and  $L_o$ .

227 Whereas the ice thickness evolution in the region of sample origin,  $H(t)$ , is a variable calculated  
 228 by the model from ice mass balance calculation (see Eq. S5 below), the ice thickness at the foothills of  
 229 Transantarctic Mountains  $H_{RE}(t)$  is used as the forcing function that is driving the temporal response of the  
 230 simulated system to climate forcing. The underlying idea is that the climate forcing, which is represented  
 231 here by isotopic records from ice cores, is driving changes in the position of the grounding lines in the Ross  
 232 Embayment and, hence also the changes in  $H_{RE}(t)$ . Ice thickness forcing at the foothills of Transantarctic  
 233 Mountains,  $H_{RE}(t)$ , is parametrized as a linear function of an ice core isotopic record of paleoclimate,  $i(t)$ ,  
 234 covering the time periods of sample precipitation:

$$235 H_{RE}(t) = H_o + C_i[i(t) - i_o] \quad \text{Eq. S4}$$

236 where  $H_o$  = is the initial thickness (taken from ice sheet model output of ref. <sup>27</sup>),  $C_i$  = proportionality  
 237 constant with units of meters per ‰, and  $i_o$  = the initial isotopic value in ‰. For simulations of basal  
 238 thermal conditions pertaining to the sample MA113 we use the  $\delta^{18}\text{O}$  record from the WAIS Divide ice  
 239 core<sup>38</sup> and for the older sample PRR50489 we use the  $\delta\text{D}$  record from the EDC ice core<sup>39</sup>. In our model the  
 240 ice thickness in the sample formation area,  $H(t)$ , evolves through time following this simple mass-balance  
 241 ODE:

$$242 \frac{\partial H(t)}{\partial t} = aL_a - UH(t) \quad \text{Eq. S5}$$

243

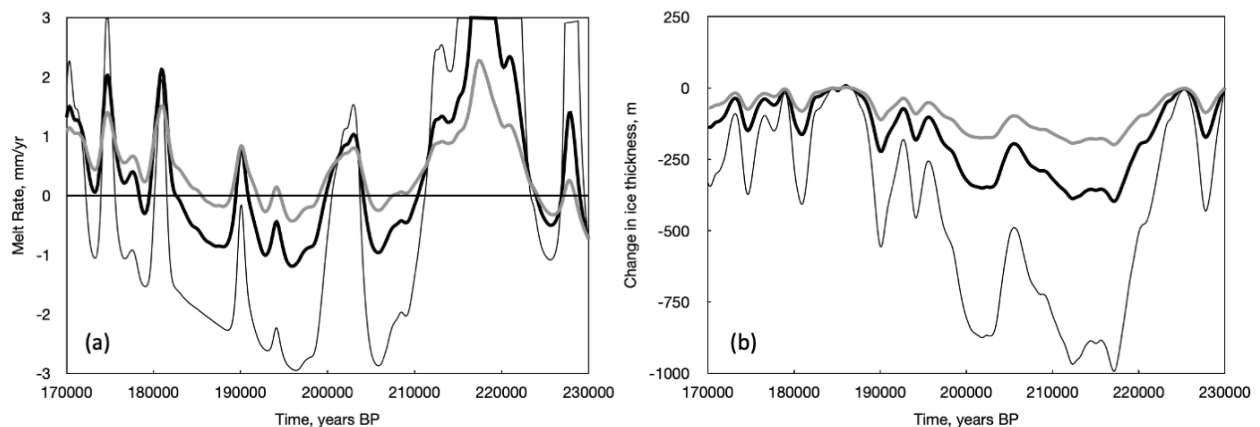
248 where  $t$  = time,  $a$  = accumulation rate (0.02-0.03 m/year taken from the ice sheet model output of ref. <sup>27</sup>),  
249 and  $L_a$  = accumulation length scale (i.e., taken to be 500 km as the approximate length of the accumulation  
250 zone upstream of the site where  $H(t)$  is evaluated. The first term on the right-hand side represents an  
251 aggregated influx of ice from upstream while the second term is an aggregated outflux of ice in downstream  
252 direction. It is important to keep in mind that in this flowline formulation of mass balance, the left-hand  
253 side of this equation is implicitly multiplied by unit width, which resolves the apparent mismatch in units  
254 between the two sides of Eq. S5. The accumulation length scale should not be taken literally (e.g., as the  
255 distance from the sample origination site to the ice divide), given the fact that there is considerable flow  
256 conversion occurring as ice flow funnels from widespread upper drainage areas towards relatively narrow  
257 valleys of outlet glaciers crossing the Transantarctic Mountains. Rather,  $L_a$  is used in our model as a  
258 flowline representation of the upstream accumulation area. We examined the sensitivity of our results to  
259 different choices of  $L_a$  ranging from dozens of kilometers to over 1000 km and got the desired oscillations  
260 in basal thermal conditions when  $L_a$  ranges between ca. 300 and 800 km. For too short  $L_a$  there was only  
261 basal freezing and for too long  $L_a$  there was only basal melting. The accumulation rate is kept constant  
262 since our model sensitivity experiments indicated that varying it with time did not materially impact the  
263 model output.

264 One concern that can be raised about the applicability of the system of equations S4 and S5 is that  
265 they do not account for any lags between the climate forcing and the glaciological response at the sample  
266 origination sites. By neglecting these lags, we assume that they are smaller than the combined dating  
267 uncertainties of the ice core timescale and the U-series-dated sample precipitation chronology. In the case  
268 of MA113, the uncertainties in the sample age model, >1.5 kyr, are clearly higher than the uncertainties in  
269 the WAIS Divide ice core record, ~0.5 kyr <sup>29</sup>. For the older sample, PRR50489, we use the EDC ice core  
270 record, which has considerably higher uncertainties, 2-4 kyrs, over the period of sample precipitation<sup>40</sup>. In  
271 general, a lag in the glaciological response to the climate forcing would have to be >2 kyrs, to justify its  
272 inclusion in our reduced-complexity model. Below we argue that plausible response timescales are shorter  
273 than this. Propagation of glaciological perturbations takes place through kinematic-wave and diffusive  
274 processes<sup>41</sup>, with the former dominating in low surface-slope areas moving through basal sliding (e.g., ice  
275 streams) and the latter in high surface-slope regions where ice motion is accommodated predominantly  
276 through internal deformation (section 11.3.3 in ref. <sup>42</sup>). As a conservative example, we will consider here  
277 the case of the MAM study area, which is located further towards the ice sheet interior than the EM region  
278 and, hence, should have longer glaciologic response times to ocean thermal forcing. Our sample precipitated  
279 in this region, MA113, formed entirely during the Marine Isotope Stage 3 when climatic conditions were  
280 colder than during the Holocene but not as cold as during the last glacial maximum<sup>43</sup>. There are no firm  
281 constraints on the position of the grounding line in the Ross Embayment during MIS 3, so for simplicity  
282 we will assume that this grounding line was, on average, at the approximate position of the front of the  
283 modern Ross Ice Shelf, with fluctuations around this position during warm and cold millennial phases. This  
284 would put the point of discharge of Law Glacier into the Ross Embayment about 600 km away from the  
285 assumed average MIS 3 grounding line position. Fast flowing ice streams crossed the grounded ice in the  
286 Ross Embayment<sup>44</sup> and we will assume that they moved with speed of ca. 0.3 km/yr, which would translate  
287 into kinematic wave speed of ca. 1 km/yr <sup>41</sup>. In this scenario, glaciological effects of grounding line  
288 migration would take about 0.6 kyrs to arrive at the mouth of Law Glacier. The lower half of this glacier  
289 moves at present with high enough velocities, ca. 0.1-0.4 km/yr to infer that it is likely sliding. Hence, we  
290 will also use here the kinematic wave speed to estimate how long it would take for a glaciological  
291 perturbation at the mouth of the glacier to propagate half-way its length, i.e., ~50 km. With assumed average  
292 speed of ca. 0.2 km/yr, the kinematic wave speed is ca. 0.7 km/yr and the 50-km travel time is ca. 0.07 kyrs.  
293 The last ca. 50 km of the glacier towards the MAM experiences slow ice motion, 0.02-0.03 km/yr,  
294 suggesting dominance of internal ice deformation and diffusive processes for propagation of glaciological  
295 perturbations. Assuming average surface slope of 0.006, ice thickness of 1 km, and average ice velocity  
296 0.02 km/yr <sup>14,18</sup>, we estimate the horizontal diffusivity to be 10 km<sup>2</sup>/yr, and a diffusional timescale of signal  
297 propagation of 0.25 kyrs over 50 km. Altogether, we estimate that it would take a grounding-line  
298 perturbation about 1 kyr to propagate from the grounding line to the MAM region. We justify the fact that

299 our equations S4 and S5 do not make a provision for this lag by the fact that 1 kyr is significantly shorter  
300 than the combined uncertainties in the chronology of our samples and of the isotopic ice core records used  
301 to force temporal variations in our model.

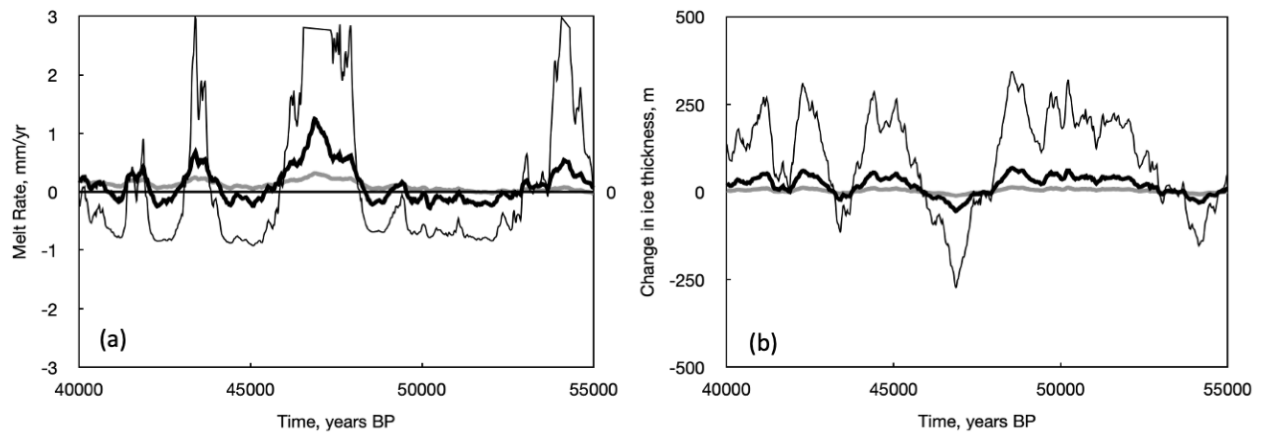
302 To produce the output shown in Figure 1 of the main manuscript text, we solved numerically the  
303 system of equations S1 through S5 using a forward-difference solver with time step of 10 years and a set  
304 of the necessary initial conditions. Each simulation was started 10,000 years before the beginning of the  
305 two precipitate records to provide model time for relaxation of the calculation from any artifacts associated  
306 with our choice of initial conditions. The basal thermal energy budget is expressed in terms of equivalent  
307 basal melting/freezing rate in units of mm/year using the volumetric latent heat of ice  $3 \times 10^8$  Joules/m<sup>3</sup>. The  
308 key tunable model parameter is  $C_i$ , the constant determining the sensitivity of ice thickness changes,  
309  $H_{RE}(t)$ , to variations in isotopic records of paleoclimate (Equation S4). We used visual inspection of  
310 outputs from dozens of sensitivity runs to evaluate which values of  $C_i$  yield satisfactory agreement with the  
311 geochemical record obtained on the two samples. The sensitivity of our results to  $C_i$  is illustrated in Figure  
312 S1(a). For the set of control parameters used to generate Figure S1a, the basal heat budget experiences  
313 switches between melting and freezing in the right time periods to explain changes between opal and calcite  
314 precipitation if the  $C_i$  parameter is between 10 and 23. A  $C_i$  value that is too low does not yield the expected  
315 melting-freezing switches in the last 15,000 years of the record (e.g.,  $C_i = 5$  in Figure S1a). A  $C_i$  value that  
316 is too high results in output that predicts freezing period between 180 and 200 kyrs BP that are too long  
317 (e.g.,  $C_i = 25$  in Figure S1a). The satisfactory results,  $C_i = 10$  to 23, are consistent with ice thickness  
318 changes in the Ross Embayment,  $H_{RE}(t)$ , of a few to several hundreds of meters on the millennial scale of  
319 AIM climate cycles. This magnitude of ice thickness variations corresponds to the cases of high sensitivity  
320 of the Antarctic ice sheet to ocean thermal forcing in numerical experiments of ref. <sup>27</sup>. Figure S2 shows  
321 equivalent results for the sample MA113, with  $C_i = 10, 50,$  and  $250$  in units of m/‰ of  $\delta^{18}O$  (since we are  
322 using the WAIS Divide ice core record for this sample). Generally, satisfactory results are obtained for  
323 MA113 when  $C_i$  is between ca. 50 and 200. A  $C_i$  value that is too low produces switches to basal freezing  
324 in the second half of the record that are too infrequent. While a  $C_i$  value that is too high misses some  
325 switches to basal melting (e.g., Figure S2). Ice thickness changes that produce satisfactory results are in the  
326 range of a few hundred meters variation in  $H_{RE}(t)$ . This range is somewhat lower than that for the other  
327 sample. However, given this more interior sample location, this result is still consistent with the ice sheet  
328 model runs of ref. <sup>27</sup> that assume high sensitivity to the ocean thermal forcing.

329  
330



331  
332  
333 **Figure S1 | Reduced Complexity Ice Sheet Model Outputs for Sample PRR50489.** a. Sensitivity of the  
334 basal thermal energy balance, expressed in terms of equivalent basal melt (+) or freeze (-) rate given in  
335 mm/year. The thick black line shows the preferred scenario for  $C_i = 10$  m per ‰ of dD from the EDC ice  
336 core record. The thin black line gives the  $C_i = 25$  scenario and the thick grey line is for the  $C_i = 5$  case. b.  
337 Equivalent changes in ice thickness,  $H_{RE}(t)$ , which represent the impact of climate forcing on our model

338 through equation S4. The same types of lines as in **a.** are used here to represent the three cases  $C_i = 5, 10$   
339 and 25.  
340  
341



342  
343  
344 **Figure S2 | Reduced Complexity Ice Sheet Model Outputs for Sample MA113.** Plots equivalent to those  
345 in Figure S1 but for simulations pertaining to the sample MA113 and with  $C_i = 10, 50,$  and 250 of m per  
346 ‰ of, corresponding to the thick grey lines, **a.** Sensitivity of the basal thermal energy balance, expressed  
347 in terms of equivalent basal melt (+) or freeze (-) rate given in mm/year. The thick black lines show the  
348 preferred scenario for  $C_i = 50$  m per ‰ of  $d^{18}O$  from the WAIS Divide ice core record. The thin black lines  
349 give the  $C_i = 250$  scenario and the thick grey lines are for the  $C_i = 10$  case.  
350

#### 351 Additional References

- 352
- 353 1. Condon, D. J., McLean, N., Noble, S. R. & Bowring, S. A. Isotopic composition  
354 (238U/235U) of some commonly used uranium reference materials. *Geochim.*  
355 *Cosmochim. Acta* **74**, 7127–7143 (2010).
  - 356 2. Hamelin, B., Bard, E., Zindler, A. & Fairbanks, R. G. 234U/238U mass spectrometry of  
357 corals: How accurate is the UTh age of the last interglacial period? *Earth Planet. Sci. Lett.*  
358 **106**, 169–180 (1991).
  - 359 3. Frisia, S. *et al.* The influence of Antarctic subglacial volcanism Maximum. *Nat. Commun.*  
360 **8**, 1–9 (2017).
  - 361 4. Cheng, H. *et al.* The half-lives of uranium-234 and thorium-230. *Chem. Geol.* **169**, 17–33  
362 (2000).
  - 363 5. Kassab, C. M. *et al.* Formation and evolution of an extensive blue ice moraine in central  
364 Transantarctic Mountains, Antarctica. *J. Glaciol.* **66**, 49–60 (2019).
  - 365 6. Bader, N. A., Licht, K. J., Kaplan, M. R., Kassab, C. & Winckler, G. East Antarctic ice  
366 sheet stability recorded in a high-elevation ice-cored moraine. *Quat. Sci. Rev.* **159**, 88–102  
367 (2017).
  - 368 7. Graly, J. A., Licht, K. J., Kassab, C. M., Bird, B. W. & Kaplan, M. R. Warm-based basal  
369 sediment entrainment and far-field Pleistocene origin evidenced in central Transantarctic  
370 blue ice through stable isotopes and internal structures. *J. Glaciol.* **64**, 185–196 (2018).
  - 371 8. Faure, G. Physical Description of the Elephant and Reckline Moraines. in *Workshop on*  
372 *Antarctic Meteorite Standing Surfaces* 24–25 (1990).
  - 373 9. Cassidy, W., Harvey, R., Schutt, J., Delise, G. & Yanai, K. The meteorite collection of  
374 Antarctica. *Meteorites* **27**, 490–525 (1992).

- 375 10. Bintanja, R. On the Glaciological, Meteorological, and Significance. *Rev. Geophys.* **37**,  
376 337–359 (1999).
- 377 11. Rhee, H. H. *et al.* Quaternary ice thinning of David Glacier in the Terra Nova Bay region,  
378 Antarctica. *Quat. Geochronol.* **67**, 101233 (2022).
- 379 12. Faure, G. & Harwood, D. M. Marine microfossils in till clasts of the Elephant Moraine on  
380 the east antarctic ice sheet. in *Antarctic Journal of the United States* 23–25 (1990).
- 381 13. Fretwell, P. *et al.* Bedmap2: Improved ice bed, surface and thickness datasets for  
382 Antarctica. *Cryosphere* **7**, 375–393 (2013).
- 383 14. Matsuoka, K. *et al.* Quantarctica, an integrated mapping environment for Antarctica, the  
384 Southern Ocean, and sub-Antarctic islands. *Environ. Model. Softw.* **140**, (2021).
- 385 15. Nishiizumi, K. Subaerial exposure ages of bedrock near meteorite stranding surfaces. in  
386 *Antarctic Meteorite Stranding Surfaces* 60–64 (1990).
- 387 16. Jull, A. J. T. Terrestrial ages of meteorites. in *Accretion of extraterrestrial matter*  
388 *throughout Earth's history* 241–266 (2001). doi:10.1038/293433a0
- 389 17. Coren, F., Delisle, G. & Sterzai, P. Ice dynamics of the Allan Hills meteorite  
390 concentration sites revealed by satellite aperture radar interferometry. *Meteorit. Planet.*  
391 *Sci.* **38**, 1319–1330 (2003).
- 392 18. Rignot, E., Mouginot, J. & Scheuchl, B. Ice flow of the antarctic ice sheet. *Science (80-. )*.  
393 **333**, 1427–1430 (2011).
- 394 19. Mouginot, J., Scheuch, B. & Rignot, E. Mapping of ice motion in antarctica using  
395 synthetic-aperture radar data. *Remote Sens.* **4**, 2753–2767 (2012).
- 396 20. Fudge, T. J. *et al.* Variable relationship between accumulation and temperature in West  
397 Antarctica for the past 31,000 years. *Geophys. Res. Lett.* **43**, 3795–3803 (2016).
- 398 21. MacAyeal, D. R. Binge/purge oscillations of the Laurentide Ice Sheet as a cause of the  
399 North Atlantic's Heinrich events. *Paleoceanography* **8**, 775–784 (1993).
- 400 22. Morse, D. L., Waddington, E. D. & Rasmussen, L. A. Ice deformation in the vicinity of  
401 the ice-core site at Taylor Dome, Antarctica, and a derived accumulation rate history. *J.*  
402 *Glaciol.* **53**, 449–460 (2007).
- 403 23. Favier, V. *et al.* An updated and quality controlled surface mass balance dataset for  
404 Antarctica. *Cryosphere* **7**, 583–597 (2013).
- 405 24. Hulbe, C. & Fahnestock, M. Century-scale discharge stagnation and reactivation of the  
406 Ross ice streams, West Antarctica. *J. Geophys. Res. Earth Surf.* **112**, 1–11 (2007).
- 407 25. Tulaczyk, S., Kamb, W. B. & Engelhardt, H. F. Basal mechanics of Ice Stream B, West  
408 Antarctica 2. Undrained plastic bed model. *J. Geophys. Res. Solid Earth* **105**, 483–494  
409 (2000).
- 410 26. Goodge, J. W. Crustal heat production and estimate of terrestrial heat flow in central East  
411 Antarctica, with implications for thermal input to the East Antarctic ice sheet. *Cryosphere*  
412 **12**, 491–504 (2018).
- 413 27. Blasco, J., Tabone, I., Alvarez-Solas, J., Robinson, A. & Montoya, M. The Antarctic Ice  
414 Sheet response to glacial millennial-scale variability. *Clim. Past* **15**, 121–133 (2019).
- 415 28. Barbante, C. *et al.* One-to-one coupling of glacial climate variability in Greenland and  
416 Antarctica. *Nature* **444**, 195–198 (2006).
- 417 29. Buizert, C. *et al.* The WAIS Divide deep ice core WD2014 chronology &ndash; Part 1:  
418 Methane synchronization (68-31 ka BP) and the gas age-ice age difference. *Clim. Past* **11**,  
419 153–173 (2015).
- 420 30. Begeman, C. B., Tulaczyk, S. M. & Fisher, A. T. Spatially Variable Geothermal Heat Flux

- 421 in West Antarctica: Evidence and Implications. *Geophys. Res. Lett.* **44**, 9823–9832  
422 (2017).
- 423 31. Cauquoin, A. *et al.* Comparing past accumulation rate reconstructions in East Antarctic  
424 ice cores using <sup>10</sup>Be, water isotopes and CMIP5-PMIP3 models. *Clim. Past* **11**, 355–367  
425 (2015).
- 426 32. Bintanja, R. On the Glaciological, Meteorological, and Climatological Significance of  
427 Antarctic Blue Ice Areas. *Rev. Geophys.* **37**, 337–359 (1999).
- 428 33. Cuffey, K. M. & Paterson, W. S. . B. *Physics of Glaciers, Fourth Edition. The Physics of*  
429 *Glaciers* (2010).
- 430 34. Ritz, C. Time dependent boundary conditions for calculation of temperature fields in ice  
431 sheets. *Int. Assoc. Hydrol. Sci.* **170**, 207–216 (1987).
- 432 35. Goehring, B. M., Balco, G., Todd, C., Moening-Swanson, I. & Nichols, K. Late-glacial  
433 grounding line retreat in the northern Ross Sea, Antarctica. *Geology* **47**, 291–294 (2019).
- 434 36. Spector, P. *et al.* Rapid early-Holocene deglaciation in the Ross Sea, Antarctica. *Geophys.*  
435 *Res. Lett.* **44**, 7817–7825 (2017).
- 436 37. Neuhaus, S. *et al.* Did Holocene climate changes drive West Antarctic grounding line  
437 retreat and re-advance? *Cryosph. Discuss.* 1–30 (2021). doi:10.5194/tc-2020-308
- 438 38. Members, W. D. P. Precise inter-polar phasing of abrupt climate change during the last ice  
439 age. *Nature* **520**, 661–665 (2015).
- 440 39. Jouzel, J. *et al.* Orbital and millennial antarctic climate variability over the past 800,000  
441 years. *Science (80-. )*. **317**, 793–796 (2007).
- 442 40. Veres, D. *et al.* The Antarctic ice core chronology (AICC2012): An optimized multi-  
443 parameter and multi-site dating approach for the last 120 thousand years. *Clim. Past* **9**,  
444 1733–1748 (2013).
- 445 41. Nye, J. F. The response of glaciers and ice-sheets to seasonal and climatic changes. *Proc.*  
446 *R. Soc. London. Ser. A. Math. Phys. Sci.* **256**, 559–584 (1960).
- 447 42. Cuffey, K. M. & Paterson, W. S. B. *The physics of glaciers.* (2010).
- 448 43. Siddall, M., Rohling, E. J., Thompson, W. G. & Waellbroeck, C. Marine isotope stage 3  
449 sea level fluctuations: Data synthesis and new outlook. *Rev. Geophys.* **46**, 1–29 (2008).
- 450 44. Anderson, J. B. *et al.* Ross Sea paleo-ice sheet drainage and deglacial history during and  
451 since the LGM. *Quat. Sci. Rev.* **100**, 31–54 (2014).
- 452